

Supporting Information

Plenty of Room at the Top: Exploiting Nanowire – Polymer Synergies in Transparent Electrodes for Infrared Imagers

*Shlok J. Paul[†], Håvard Mølnås[†], Steven L. Farrell, Nitika Parashar, Elisa Riedo, and
Ayaskanta Sahu**

[†]These authors contributed equally to this manuscript.

Section 1: Thermogravimetric analysis

Thermogravimetric analysis (TGA) was used to determine the achieved Ag-NW content in the Ag-NW-PVA composite films. **Figure S1** shows the TGA spectra for Ag-NW with polyvinylpyrrolidone (PVP) ligands based on the stock solution and pure PVA polymer (Figure S1a), as well as the 20 wt% Ag-NW in PVA mixed solution and film post vacuum treatment (Figure S1b). The residual carbon (C) content of PVA after air-free heat treatment approximately matches the PVP content in the Ag-NWs. A higher residual Ag-NW content than theoretically estimated based on mass ratios was measured in the 20 wt% Ag-NW-PVA mixed solution. This could be due to higher Ag-NW concentration or lower PVA concentration in the stock solutions. Due to the density difference between dissolved PVA and Ag-NWs, an even higher residual mass is measured for the films than in the mixed solution, as a higher fraction of Ag-NWs than PVA appears to stick to the substrate. Thus, the resulting films from the nominally 20 wt% Ag-NW-PVA mixed solution contain approximately ~50 wt% Ag-NW.

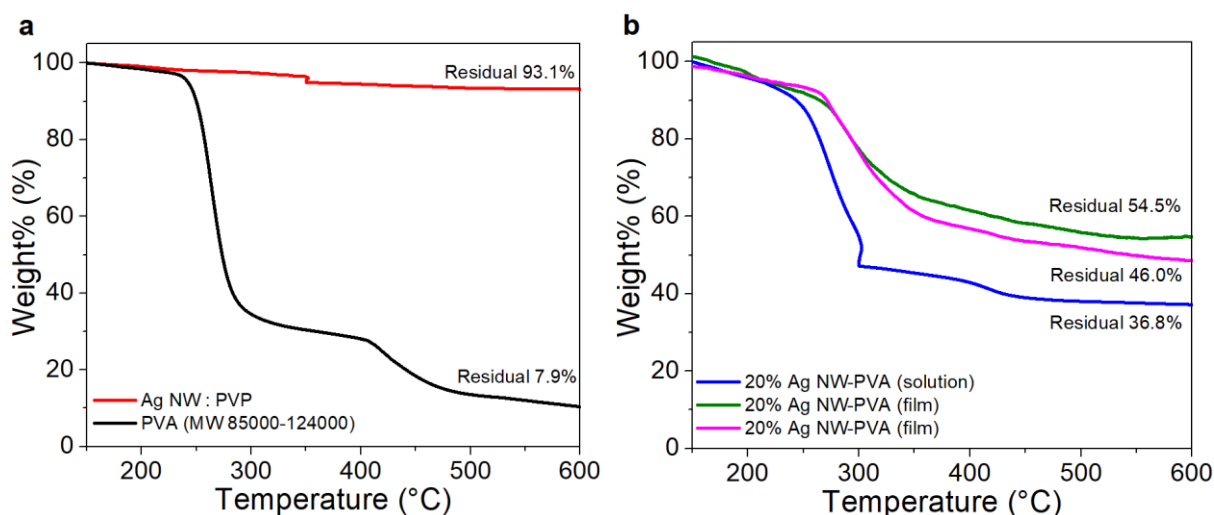


Figure S1. TGA spectra. (a) 100% Ag-NW:PVP and 100% PVA (MW 85,000-124,000). (b) 20 wt% Ag-NW-PVA composite mixed solution and films

Section 2: Additional optical measurements of Ag-NW PVA mixture

Figure S2 shows the results of an evaluation of NW area in 2D section of Ag-NW-PVA composite films using ImageJ software. The area covered by Ag-NWs increased with increasing theoretical Ag-NW loading, as expected.

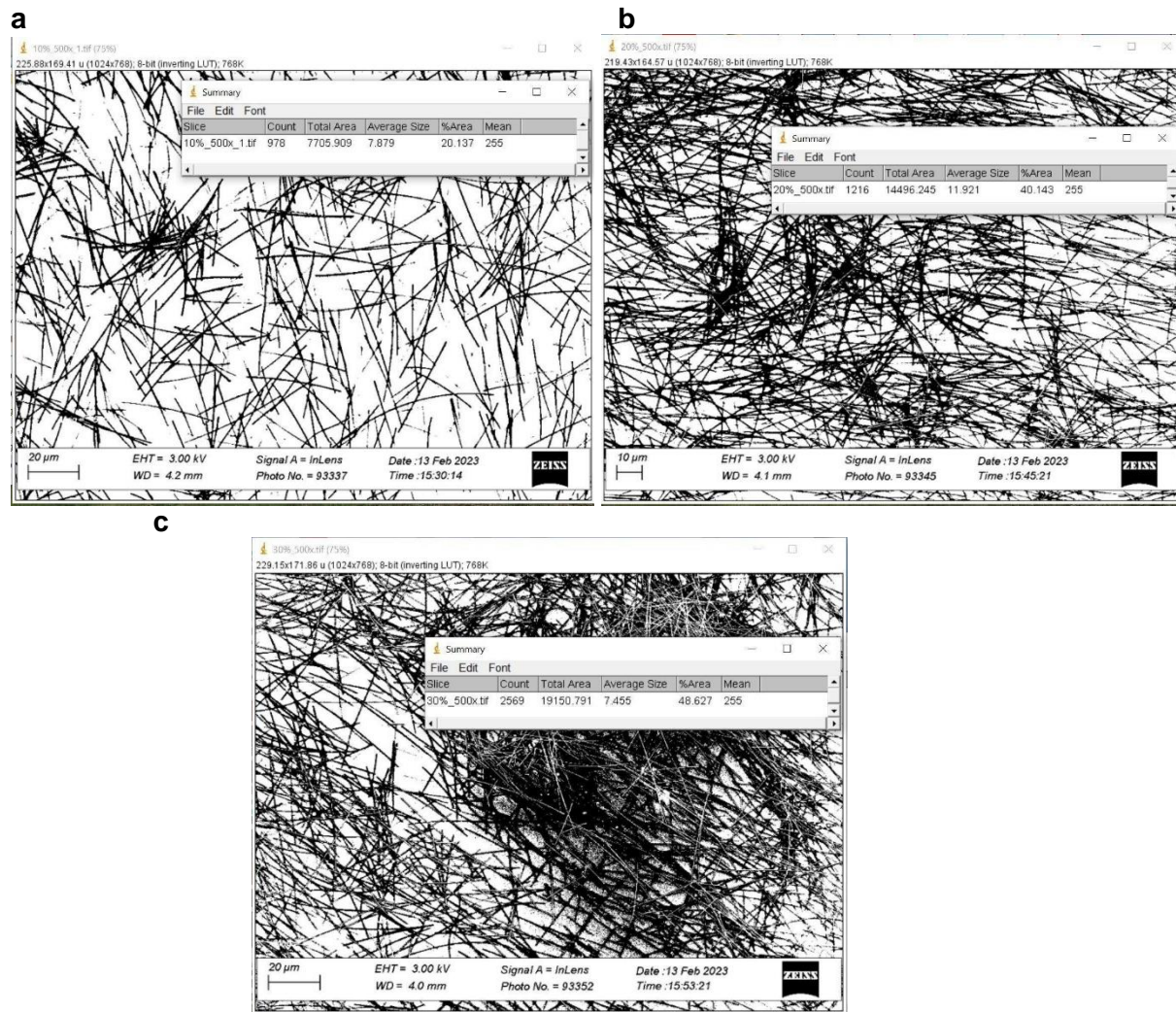


Figure S2. Evaluation of NW area in 2D sections of Ag-NW-PVA composite films using ImageJ software. (a) 10 wt% Ag-NW. Ag-NWs cover 20.1% of the area. (b) 20 wt% Ag-NW. Ag-NWs cover 40.1% of the area. (c) 30 wt% Ag-NW. Ag-NWs cover 48.6% of the area.

Figure S3 shows additional transmittance results for films spin coated from 100% PVA stock solution and 100% Ag-NW stock solution (Figure S3a), as well as Ag-NW-PVA composite films from dynamically and statically deposited 10 wt% and 20 wt% Ag-NW mixed solutions before and after vacuum treatment (Figure S3b). While 100% PVA has almost complete transmittance up to 2800 nm, the 100% Ag-NW film has peak transmittance of 65% at 1000 nm. The Ag-NW-PVA composite films show increased transmittance after vacuum treatment, likely due to removal of trapped solvents scattering incoming radiation.

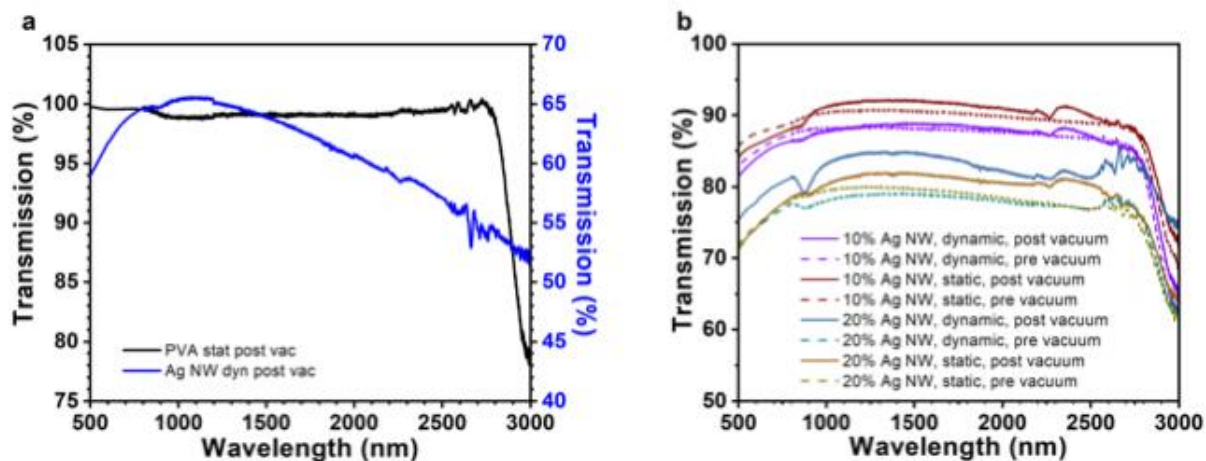


Figure S3. Transmittance for 100% PVA and 100% Ag-NW and Ag-NW-PVA films before/after vacuum treatment. (a) Pure PVA (0% Ag-NW, black curve) and Ag-NW stock solution (20 mg/mL in IPA, blue curve). (b) Ag-NW-PVA films before (dashed curves) and after (solid curves) vacuum treatment. Films display increased transmittance after vacuum treatment, likely due to removal of trapped solvent potentially scattering incoming light.

Figure S4 compares the transmittance of a film spin coated from theoretically 20 wt% Ag-PVA mix solution with a film based on 20 mg mL⁻¹ Ag-NW stock solution as well as a 20 nm Ag thermally deposited thin-film. The composite film is significantly more transmissive than the other two films from the visible range to the MWIR range.

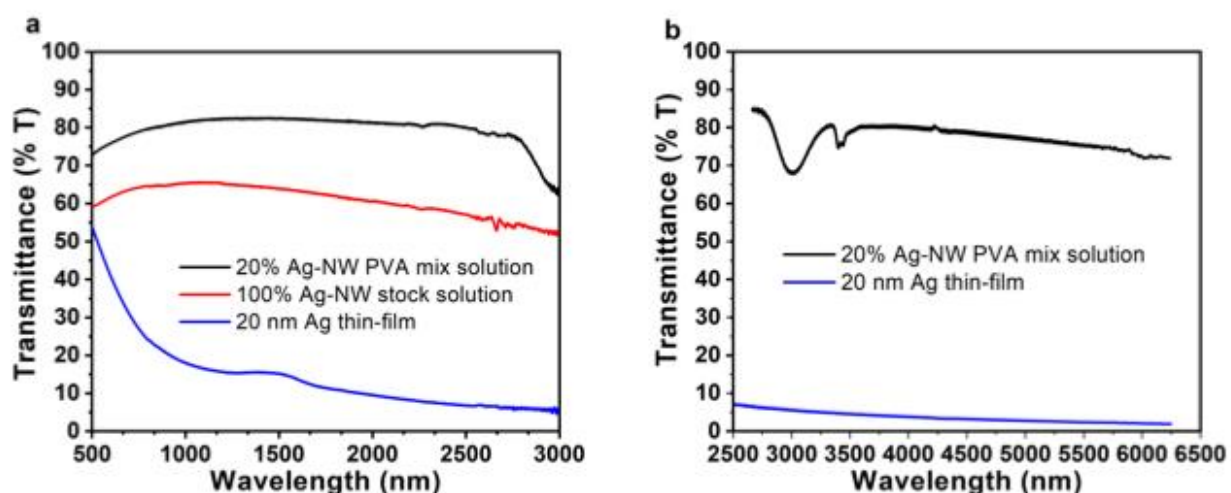


Figure S4. Comparison of transmittance for theoretical 20 wt% Ag-NW - PVA composite film (black) with film based on 100% Ag-NW stock solution (red) and 20 nm thermally deposited Ag thin-film (blue) in the visible-NIR-SWIR (a) and the Extended SWIR-MWIR (b). The composite film is significantly more transmissive than the other two films.

Section 3: Thickness measurements

Figures S5, S6 and S7 show film thickness determination through AFM measurements for 10 wt%, 20 wt% and 30 wt% theoretical Ag-NW loading, respectively. The average film thicknesses decrease from 349 nm to 144 nm to 57 nm with increasing Ag-NW loading due to decreasing mixed solution viscosity while keeping spin coating parameters constant. In the topographical images, the Ag-NWs ($\varnothing 120$ nm) can be observed protruding out of the PVA matrix.

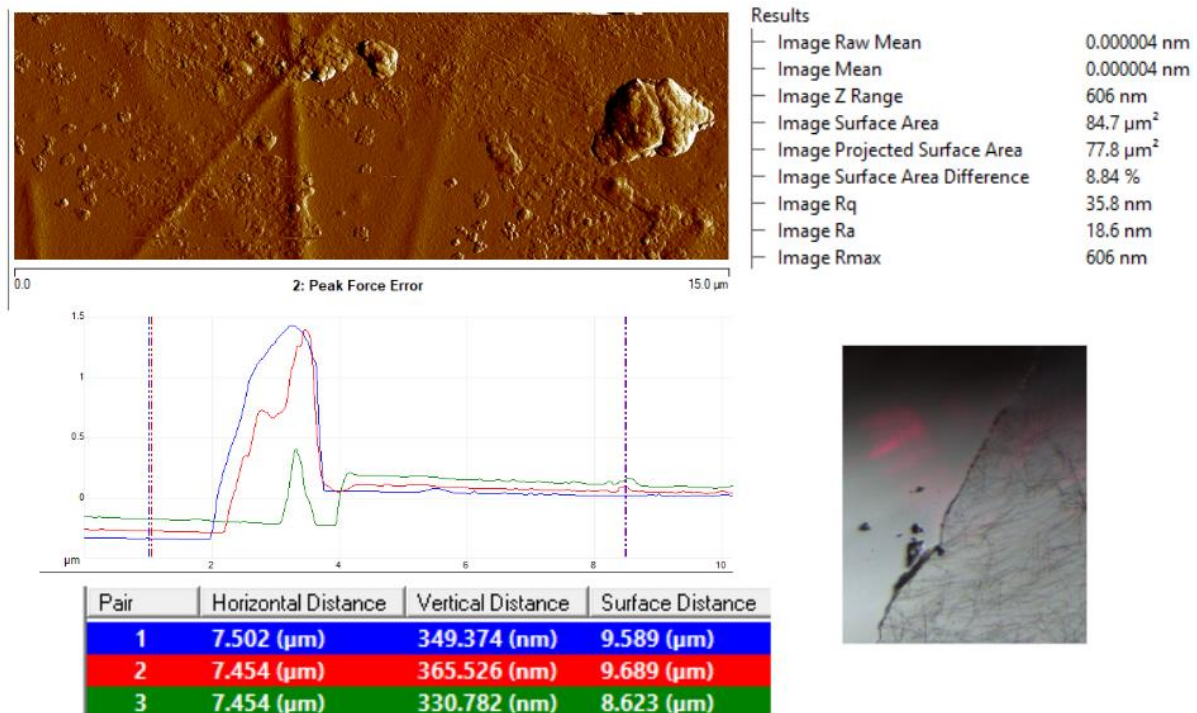


Figure S5. AFM evaluation of 10 wt% Ag-NW-PVA film on glass. Average thickness 348.6 nm.

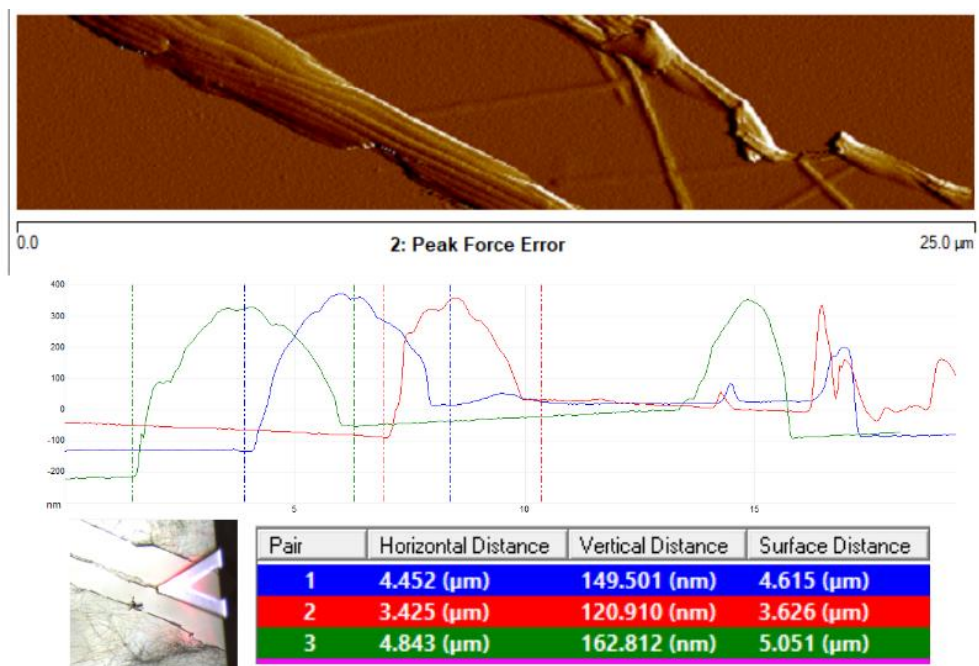


Figure S6. AFM evaluation of 20 wt% Ag-NW-PVA film on glass. Average thickness 144.4 nm.

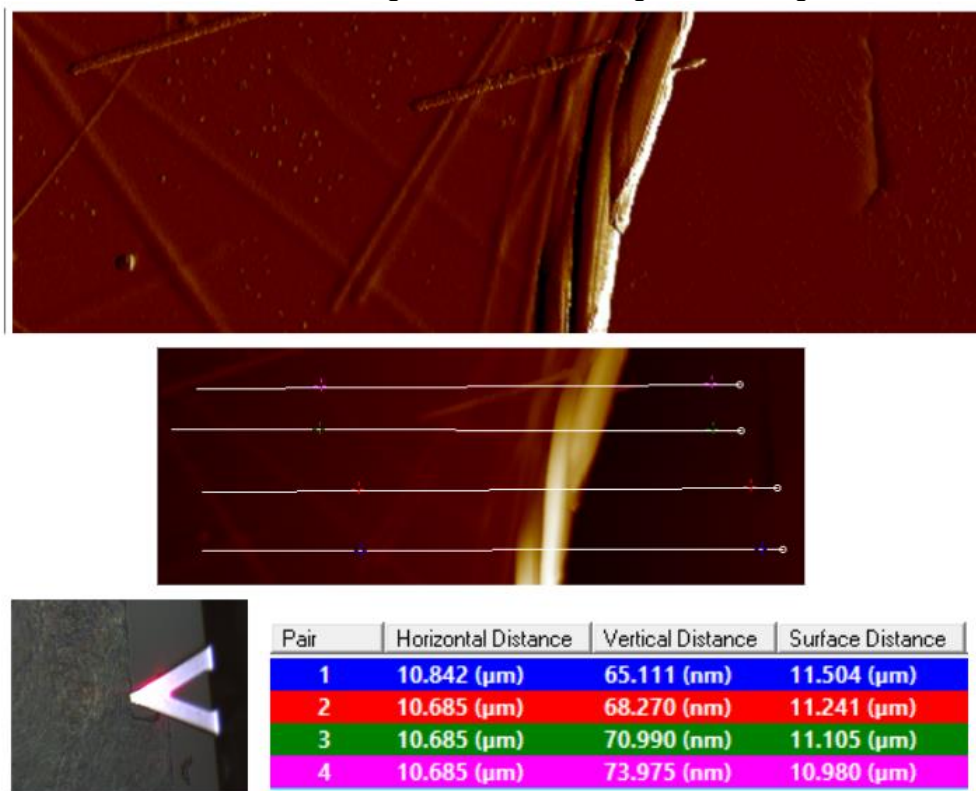


Figure S7. AFM evaluation of 30 wt% Ag-NW-PVA film on glass. Average thickness 45.6 nm / 69.1 nm.

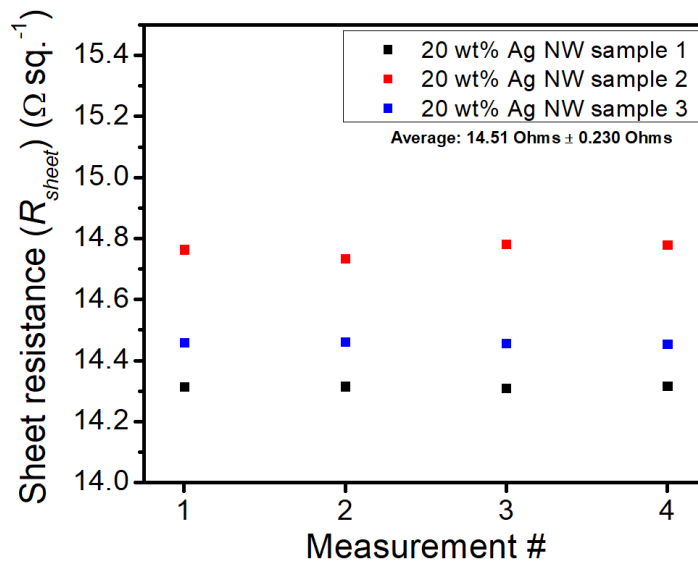
Section 4: Additional sheet resistance data

There is some scatter in the data below 15 wt% Ag-NW content. We believe this could potentially be due to insufficient amount of Ag-NWs in the composite film preventing the formation of a percolating network for charge transport. However, post a critical concentration of nearly 15-20 wt% Ag-NW, the composite is reproducible with its optoelectronic properties (both within a single set and across multiple sets of data with experiments performed across a time span over a year). Thus, we chose to fabricate devices with 20 wt% Ag-NWs.

To further demonstrate stabilization above 15 wt% Ag-NW content, three identical samples with a theoretical 20 wt% Ag-NW in PVA were fabricated. R_{sheet} was determined through four consecutive measurements per sample, allowing for statistical analysis both of the measurement error as well as sample to sample variation, as shown in **Table S1** and **Figure S8**. The average R_{sheet} for the 20wt % sample was found to be $14.51 \Omega \text{ sq.}^{-1}$ with a standard deviation of ± 0.23 (1.6%), indicating a low and stable R_{sheet} for composite films at this Ag-NW content.

Table S1. Statistical considerations for three identical samples with 20 wt% Ag-NW in PVA

Sample #	Measurement #	R_{sheet} [Ω sq. ⁻¹]	Sample average R_{sheet} [Ω sq. ⁻¹]	Set average R_{sheet} [Ω sq. ⁻¹]	Variance	Standard deviation						
1	1	14.3143	14.314	14.51	0.04	0.23						
	2	14.3156										
	3	14.309										
	4	14.317										
2	1	14.7644	14.7649				14.51	0.04	0.23			
	2	14.7339										
	3	14.7816										
	4	14.7798										
3	1	14.46	14.46							14.51	0.04	0.23
	2	14.4621										
	3	14.4562										
	4	14.4539										

**Figure S8.** R_{sheet} for three new, identical Ag-NW-PVA composite films with theoretical 20 wt% Ag-NW measured through four consecutive and repositioned measurements. R_{sheet} was determined through the 4-probe van-der-Pauw method.

Section 5: Comparison of performance with traditional TCE materials

The Ag-NW-PVA films show comparable performance to traditional TCE materials; 80 nm FTO has a reported R_{sheet} of 70 - 90 Ω sq.⁻¹,¹ while 50 nm ITO has an $R_{sheet} \leq 40$ Ω sq.⁻¹, both on 1.1 mm glass. R_{sheet} contributes to the contact resistance, R_C , and thus the series resistance, R_s , of a photodiode, a parameter one generally aims to minimize and ensure is lower than the shunt resistance, R_{Sh} , in order to maximize the conversion efficiency.² Literature reports for 50 and 100 nm ITO films on glass and sapphire substrates show increasing absorbance throughout the SWIR range and more than 50% absorbance in the MWIR range.^{3,4} Transmission plots for 70 nm and 200 nm FTO films on glass paint the same picture.⁵ By increasing the oxide layer thickness, the R_{sheet} of ITO and FTO can be decreased, although increased thickness has been shown to negatively affect the transmittance properties.^{1,3} Our analysis of commercially available ITO and FTO films with comparable R_{sheet} to an Ag-NW-PVA film with 20% Ag-NW loading, shown in **Figure S9**, demonstrate that for ITO on glass with a R_{sheet} of 10 Ohm sq.⁻¹, the transmittance is <20% above 1700 nm, while for FTO on glass with $R_{sheet} < 14$ Ohm sq.⁻¹, the transmittance is <40% above 1700 nm. 1.1 mm glass has a transmittance of ~90 % up to 2700 nm,³ thus for the above-mentioned ITO and FTO films, the conductive oxides are the main cause of reduced transmittance.

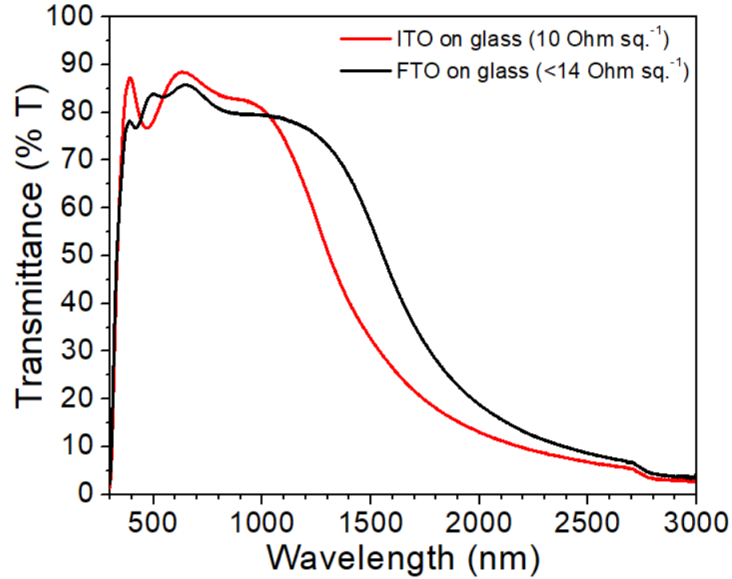


Figure S9. Transmittance of ITO and FTO films with R_{sheet} 10-14 Ohm sq.⁻¹ on glass. Significantly reduced transmittance in the SWIR is observed.

The work function of our Ag-NW-PVA composite electrode was determined to - 4.613 eV relative to vacuum based on KPFM measurements, **Figure S10**. Comparing with the known work functions of ITO and metallic Ag, both 4.7 eV,^{6,7} our electrode provides a slightly higher driving force for hole transfer. Compared to the work function of FTO, 4.4 - 4.5 eV,^{8,9} our electrode provides a slightly lower driving force for hole transfer. The stack band diagrams for all investigated device architectures are presented in Section 6 in the SI.

KPFM of Ag nanowires

$$\varphi^{sample} = \varphi^{tip} + e \cdot CPD_{sample}$$

$$\text{Measure CPD} = -0.067 \text{ V}$$

$$\varphi^{sample} = 4.68 \text{ eV} + e(-0.067)$$

$$\varphi^{sample} = 4.613 \text{ eV}$$

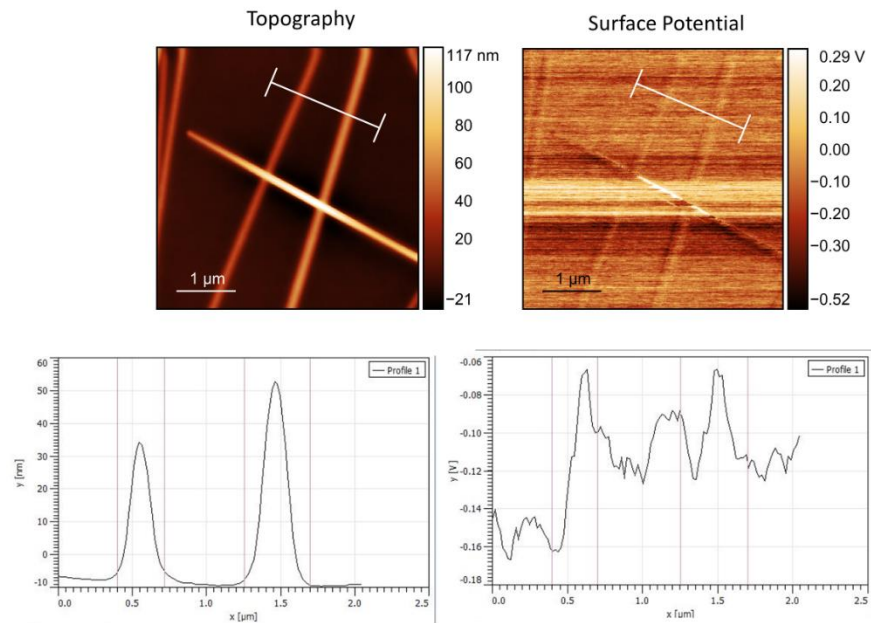


Figure S10. KPFM of Ag-NW-PVA composite for work function (φ) determination.

Section 6: Photodetector data

Figure S11 a-c) show side and top views of the main vertical device architecture utilized in this manuscript, based on commercially available S162 interdigitated electrode (IDE) glass substrates from Ossila. Each substrate contains multiple (up to 10) devices with an area on the order of $\sim 4 - 5.5 \times 10^{-3} \text{ cm}^2$, utilizing contact pads on either side of the substrate, as demonstrated in Figure S11d). The Ag-NW-PVA top contact was deposited in the area in the center of the substrate not masked off by polyimide (Kapton) tape. The unmasked areas at the left and right sides of the substrates were exposed only immediately prior to the photoresponse measurements. For control experiments, the top Ag-NW-PVA layer was replaced or modified in order to explore a hypothesis, such as for comparing the performance of Ag-NW-PVA composite top electrode to traditional thermally evaporated Ag, Figure S11c). **Table S2** shows dipping speeds, solution

concentrations and number of repetitions utilized during device fabrication using a custom-built dip coater.

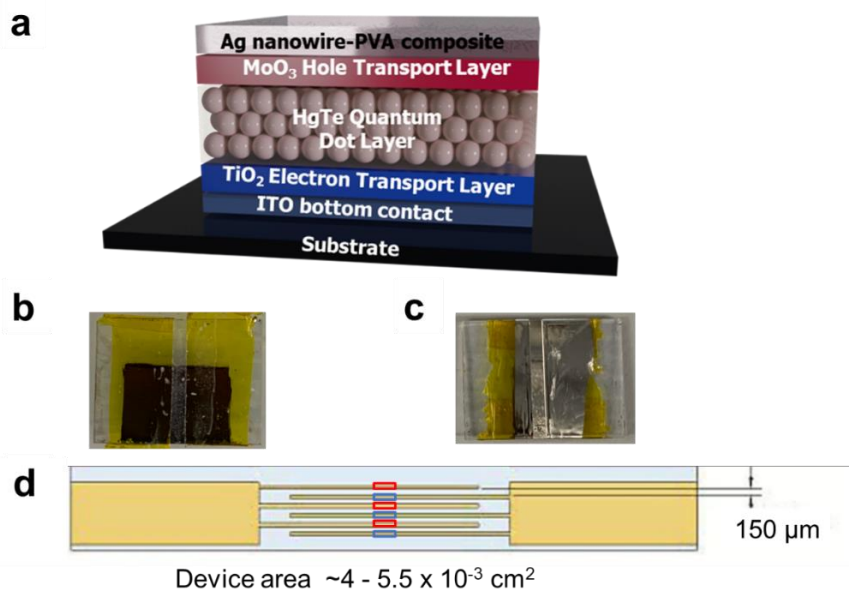


Figure S11. Device geometry and optical images of vertical HgTe devices. a) Side view of vertical device geometry. b) Top view of device with Ag-NW-PVA top contact. c) Top view of device with thermally evaporated Ag top contact. d) Active device areas ($\sim 4\text{-}5.5 \times 10^{-3} \text{ cm}^2$), utilizing interdigitated electrode architecture of prefabricated S162 Ossila substrates, are indicated by the red and blue rectangles. Image in panel (d) remains the copyright of Ossila. Adapted with permission from www.ossila.com.

Table S2. Dipping parameters for ligand exchanged HgTe CQD films

Device (Figure #)	Beaker 1 (active layer) speed (mm min ⁻¹)	Beaker 2 (ligand exchange) speed (mm min ⁻¹)	Beaker 3 (rinse) speed (mm min ⁻¹)	Hold time in beaker 2 (s)	# of repetitions	EDT/HCl ligand exchange concentration in IPA (mol L ⁻¹)
Figure 4 (Main text) and Figure S13	100	600	110	3	40	1.43×10^{-2}
Figure 5a (Main text)	70	2000	200	5	40	6.49×10^{-3}
Figure S14 (in SI)	100	400	110	6	60	9.51×10^{-3}
Figure S15 (in SI)	150	400	150	4	60	8.65×10^{-3}

Figure S12 presents band diagrams of the different device architectures utilized in this report. Replacing metallic Ag electrode with Ag-NW-PVA composite electrode (Figure S.13a-b) introduces a slightly higher driving force for hole transfer from the MoO₃ HTL to the electrode, although we expect the difference in transmittance to be the main reason for improved performance in this case. Replacing the MoO₃ HTL with Ag₂Te introduces a higher (+0.5 eV VS -0.1 eV) driving force for hole transfer from the HgTe CQDs. However, there is still a small barrier for the electrons to travel from the CQD layer to the ITO electrode. Replacing the TiO₂ ETL with SnO₂ ETL reduces or removes this barrier, which is expected to yield improved photoresponse, as observed in the final device in Figure 5 in the main text.

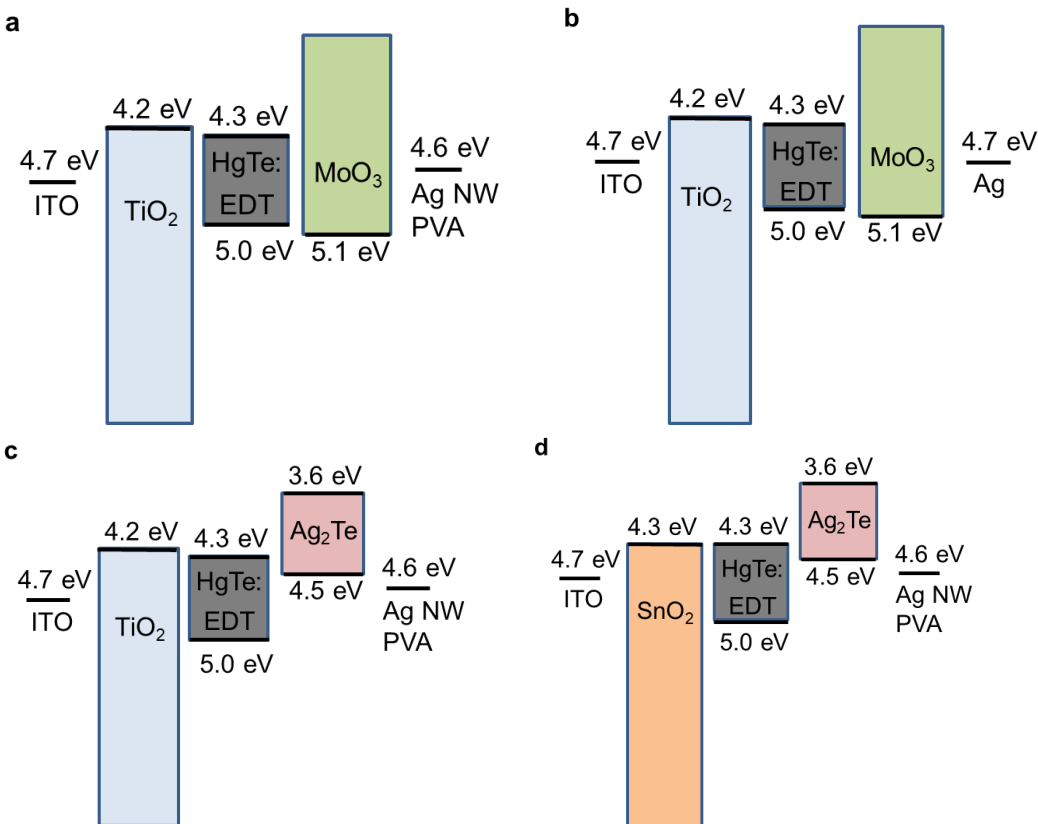


Figure S12. Stack band diagrams of all device architectures utilized in this report. With the exception of the work function of Ag-NW-PVA, which was determined in this report, all band edges and work functions are taken from literature: ITO,⁶ Ag,⁷ TiO₂,¹⁰ HgTe:EDT,¹¹ MoO₃,¹² Ag₂Te.¹³

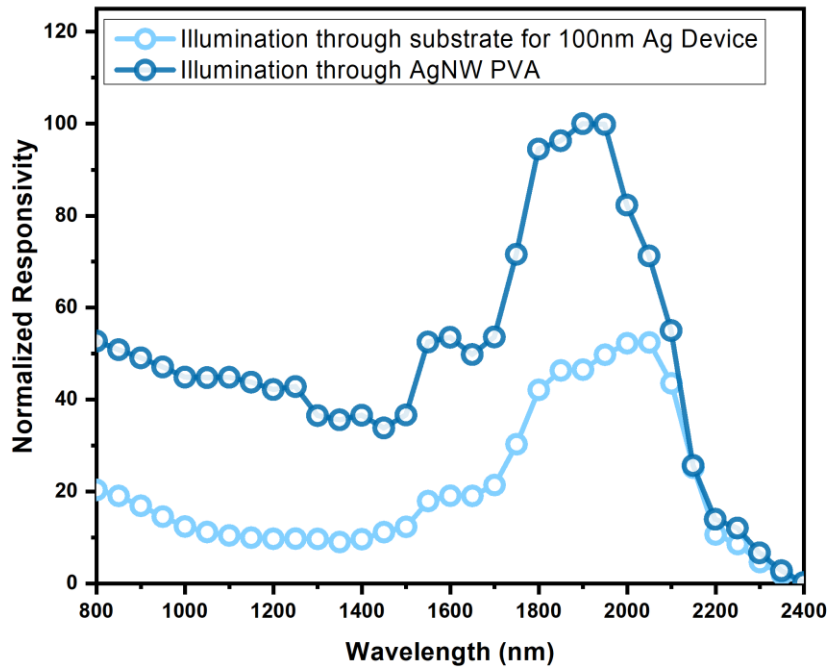


Figure S13 compares the performance of devices with 20wt% AgNW when illuminated through the top and 100 nm Ag when illuminated through the ITO to show the difference in performance between the two diodes without transparency limitations.

Figure S14 compares the performance of devices with theoretical 20 wt% Ag-NW-PVA top contact with devices with Ag-NW mesh top contact. The devices with 20 wt% Ag-NW loading outperform the other devices, illustrating the benefit of encapsulating the Ag-NWs in a PVA matrix.

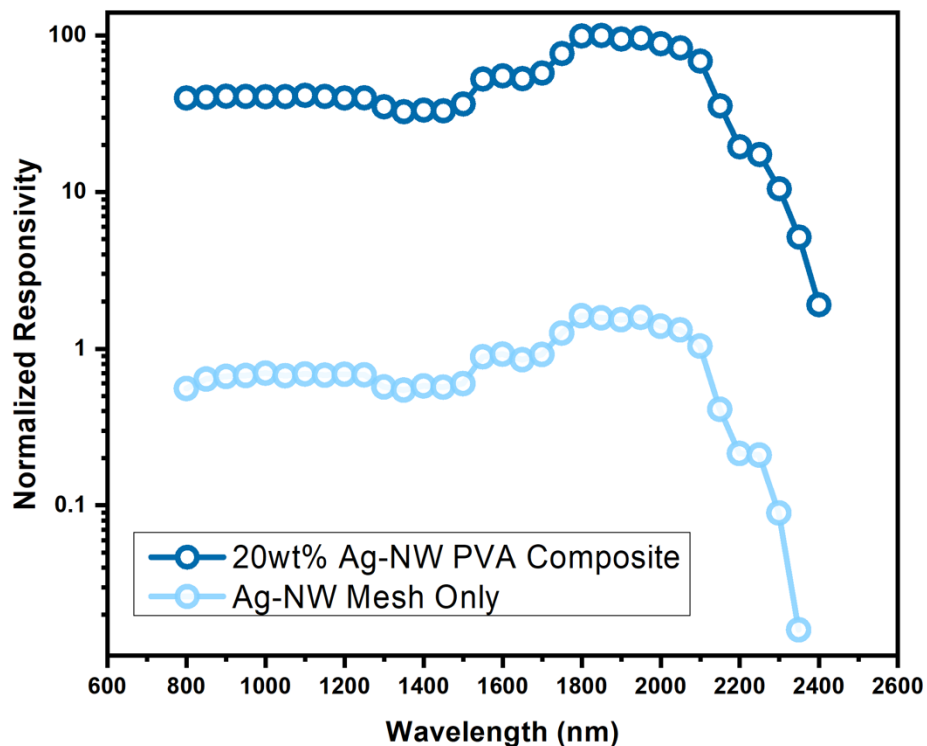


Figure S14. Normalized responsivity for comparison at 0V applied bias for a HgTe CQD vertical device with a Ag-NW mesh (no PVA) top contact compared to an identical device with 20 wt% Ag-NW-PVA composite top contact on day 1 after fabrication. Illumination through top contact. Device areas were $\sim 5 \times 10^{-3} \text{ cm}^2$.

Figure S15 compares the performance of devices with theoretical 20 wt% Ag-NW-PVA top contact deposited from a mixed solution or sequentially. Devices having a top contact deposited from mixed solution outperform devices with sequential deposition of the top contact, illustrating the benefit of spatial distribution of Ag-NWs in the PVA matrix.

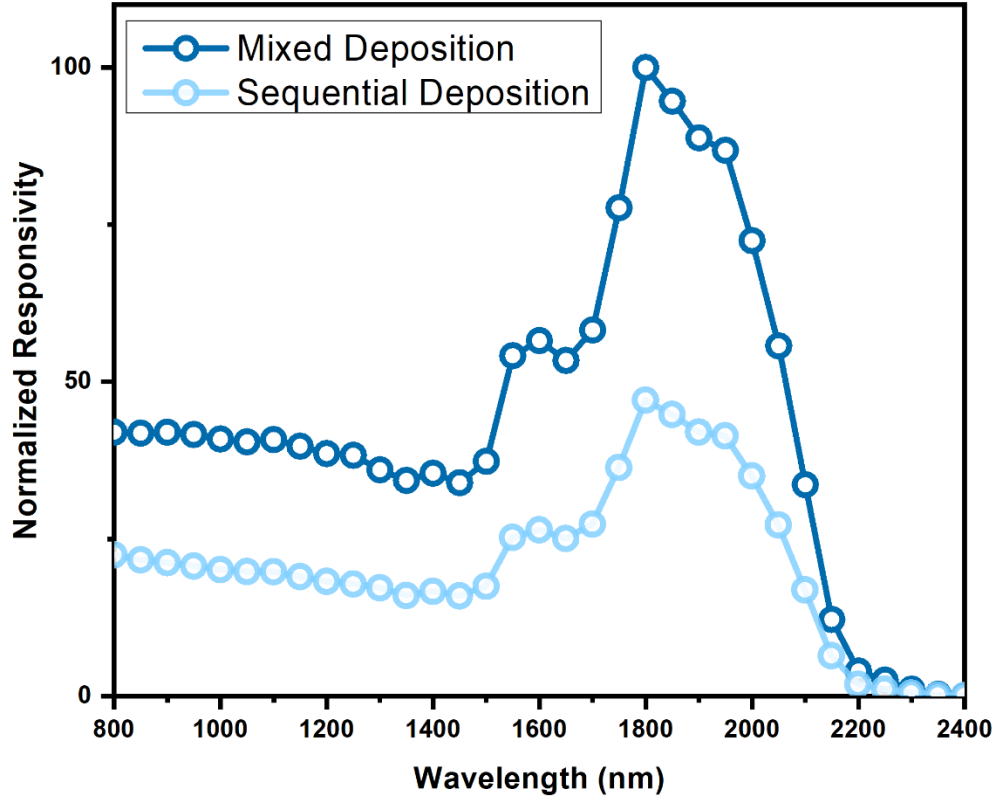


Figure S15. Normalized responsivity for comparison at 0V applied bias for a HgTe CQD vertical device with a 20 wt% Ag-NW PVA top contact deposited as a composite compared to an identical device where the Ag-NW is deposited first followed by a layer of PVA measured on day 1 from fabrication. Illumination through top contact. Device areas were $4.1 \times 10^{-3} \text{ cm}^2$.

The series resistance, R_s , and shunt resistance, R_{sh} , of the optimized diode in figure 5 of the main text was determined through fitting to the diode equation (Equation S1) using Origin software and the modified LambertW Function:

$$I = I_0 \left(e^{\frac{V - IR_s}{nV_T}} - 1 \right) + \frac{V - IR_s}{R_{sh}} \quad (\text{S1})$$

where I is the diode current, I_0 is the reverse saturation current, V is the applied voltage, n is the ideality factor, and V_T is the thermal voltage.

In the dark, R_s and R_{sh} were determined to 5.3 k Ω and 1.2 M Ω , respectively, with R^2 equal to 0.99914, indicating a very good fit, **Figure S16**. The high R_{sh} to R_s ratio and the corresponding non-linear and rectifying nature of the devices J-V curve matches well with the observations of Peterson et al.²

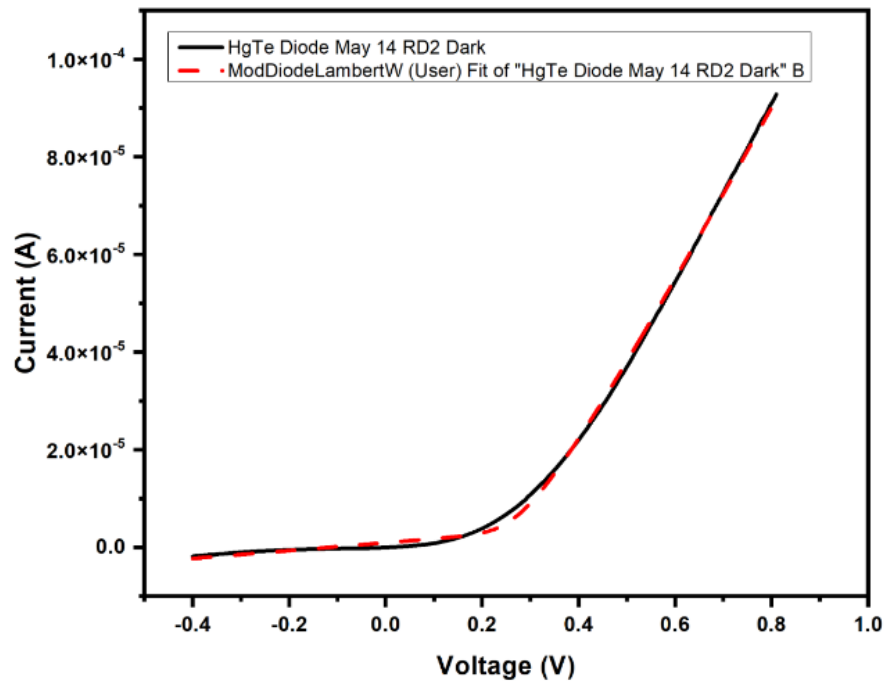


Figure S16. Result of fitting I-V curve in the dark to the diode equation

Table S3 compares the values for dark current density, R_s and R_{sh} for our optimized photodiode with comparable device stacks reported in literature. The performance of our best diode is comparable to the performance of HgTe CQD devices reported in literature, including having one of the highest R_{sh} to R_s ratios. Our reported dark current density at 0.1 V reverse bias is on the same order of magnitude as comparable SWIR HgTe CQD photodiodes operating at room temperature. **The Ag-NW-PVA top contact utilized in our device in order to achieve compatibility with imagers**

can therefore not be considered to have negatively affected the rectifying nature of our HgTe CQD photodiode.

Table S3. Comparison of dark current, shunt resistance and series resistance for HgTe CQD based photodiodes with comparable device stack.

IR-range	Device area [mm ²]	Dark current @-0.1V bias, RT [mA cm ⁻²]	Shunt resistance [Ω]	Series resistance [Ω]	Ratio R _{sh} /R _s	Reference
MWIR	0.0025 0.25	330 125	Not reported	2300-6750 150-360	N/A	2
MWIR	0.6	> 1	300 000	400	750	16, 17
MWIR	0.6 (TiO ₂ ETL)	0.5 - 5 (@80 K)	15 000 - 200 000	400 - 6000	~35	17
MWIR	0.6 (SnO _x ETL)	< 1 (@80 K)	30 000	2500	12	17
MWIR	0.6 (MoO _x HTL, Ni/Au contact)	~2 (@80 K)	10 000	1000	10	17
MWIR	0.6 (HgTe "HTL")	0.4 - 0.7 (@80 K)	100 000 - 200 000	4000 - 8000	25	17
SWIR	0.05 (no ETL) 0.05 (SnO ₂ ETL)	10 0.02	Not reported	Not reported	N/A	18
SWIR	1 (HgCl ₂ - treated)	< 1	9200	200	46	17
SWIR	4.14 (Bi ₂ S ₃ ETL) 4.14 (+blended Ag _x Hg _{1-x} Te HTL)	~0.121 ~0.002	Not reported	Not reported	N/A	19
SWIR	0.3	0.085	1 200 000	5300	226	<i>This work</i>

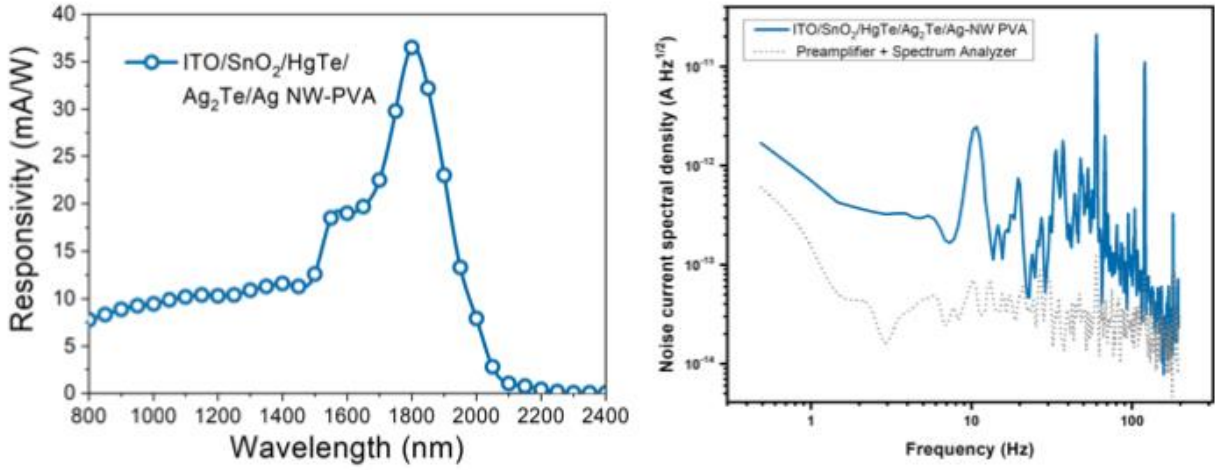


Figure S17. (a) Responsivity and (b) Noise current spectral density of figure 5 in main text.

Table S4. Photoresponse SWIR HgTe CQD photodiodes at 300K

Cutoff [μm]	Bias [V]	Responsivity [A W^{-1}]	Detectivity [Jones]	Fall Time	Reference
2.5	0	0.0025	3×10^9	370 ns *	20
2.5	0	0.25	3×10^{10}	260 ns	21
2.2	0	1	6×10^{10}	~1 us	22
2.0	0	0.13 ^{a)}	$2 \times 10^{10*}$	110 ns *	23
2.5	-0.3	0.28 ^{b)}	6×10^{10}	2.5 us	25
2	0	0.3	5×10^{10}	300 ns *	18
2	0	0.8	9×10^{10}	200 ns *	26
1.7	0	0.6	3.4×10^{11}	19 us	19
1.7	0	0.38	3.9×10^{11}	25.4 us	27
2.2	0	0.29	10^{11}	8.92 us	28
1.9 2.5	0	0.8 0.9	5.3×10^{11} 6.0×10^{11}	-	6
1.8	0	0.0365	2.9×10^{11}	23 us	This work

^{a)} with resonator ^{b)} calculated *Measured transient photocurrent decay by ns pulsed laser

References:

1. Solems, Transparent conductive oxides, https://www.solems.com/wp-content/uploads/FTO_ITO_18-2.pdf
2. J. C. Peterson and P. Guyot-Sionnest, *ACS Appl. Mater. Interfaces*, 2023, **15**, 19163. DOI 10.1021/acsami.3c00487
3. A. Jagtap, N. Goubet, C. Livache, A. Chu, B. Martinez, C. Gréboval, J. Qu, E. Dandeu, L. Becerra, N. Witkowski, S. Ithurria, F. Mathevet, M. G. Silly, B. Dubertret and E. Lhuillier, *J. Phys. Chem. C*, 2018, **122**, 14979. DOI 10.1021/acs.jpcc.8b03276
4. T. H. Dang, M. Cavallo, A. Khalili, C. Dabard, E. Bossavit, H. Zhang, N. Ledos, Y. Prado, X. Lafosse, C. Abadie, D. Gacemi, S. Ithurria, G. Vincent, Y. Todorov, C. Sirtori, A. Vasanelli and E. Lhuillier, *Nano Lett.*, 2023, **23**, 8539. DOI 10.1021/acs.nanolett.3c02306
5. R. Alchaar, C. Dabard, D. Mastrippolito, E. Bossavit, T. H. Dang, M. Cavallo, A. Khalili, H. Zhang, L. Domencah, N. Ledos, Y. Prado, D. Troadec, J. Dai, M. Tallarida, F. Bisti, F. Cadiz, G. Patriarche, J. Avila, E. Lhuillier and D. Pierucci, *J. Phys. Chem. C*, 2023, **127**, 12218. DOI 10.1021/acs.jpcc.3c01603
6. M. Chen, X. Xue, T. Qin, C. Wen, Q. Hao and X. Tang, *Adv. Mater. Technol.*, 2023, **8**, 2300315. DOI 10.1002/admt.202300315
7. J. Meng, J. A. Röhr, H. Wang, B. E. Sartor, D. Song, A. Katzenberg, M. A. Modestino, Z. Xu, J. Kong and A. D. Taylor, *Solar RRL*, 2022, **6**, 2100794.
8. M. Kim, I.-w. Choi, S. J. Choi, J. W. Song, S.-I. Mo, J.-H. An, Y. Jo, S. Ahn, S. K. Ahn, G.-H. Kim and D. S. Kim, *Joule*, 2021, **5**, 659.
9. A. K. Jena, A. Kulkarni and T. Miyasaka, *Chem. Rev.*, 2019, **119**, 3036.
10. N. Graddage, J. Ouyang, J. Lu, T.-Y. Chu, Y. Zhang, Z. Li, X. Wu, P. R. L. Malenfant and Y. Tao, *ACS Appl. Nano Mater.*, 2020, **3**, 12209. DOI 10.1021/acsanm.0c02686
11. A. Chu, B. Martinez, S. Ferré, V. Noguier, C. Gréboval, C. Livache, J. Ou, Y. Prado, N. Casaretto, N. Goubet, H. Cruguel, L. Dudy, M. G. Silly, G. Vincent and E. Lhuillier, *ACS Appl. Mater. Interfaces*, 2019, **11**, 33116. DOI 10.1021/acsami.9b09954
12. T. Hori, T. Shibata, V. Kittichungchit, H. Moritou, J. Sakai, H. Kubo, A. Fujii and M. Ozaki, *Thin Solid Films*, 2009, **518**, 522. DOI 10.1016/j.tsf.2009.07.044
13. J. Ouyang, N. Graddage, J. Lu, Y. Zhong, T.-Y. Chu, Y. Zhang, Z. Wu, O. Kodra, Z. Li, Y. Tao and J. Ding, *ACS Appl. Nano Mater.*, 2021, **4**, 13587. DOI 10.1021/acsanm.1c03030
14. R. Saran and R. J. Curry, *Nat. Photon.*, 2016, **10**, 81. DOI 10.1038/nphoton.2015.280
15. T. Nakotte, S. G. Munyan, J. W. Murphy, S. A. Hawks, S. Kang and J. Han, *J. Mater. Chem. C*, 2022, **10**, 790. DOI 10.1039/d1tc05359k

16. M. M. Ackerman, X. Tang and P. Guyot-Sionnest, *ACS Nano*, 2018, **12**, 7264. DOI 10.1021/acsnano.8b03425
17. M. M. Ackerman, PhD thesis, University of Chicago, 2020
18. C. Gréboval, E. Izquierdo, C. Abadie, A. Khalili, M. Cavallo, A. Chu, T. H. Dang, H. Zhang, X. Lafosse, M. Rosticher, X. Z. Xu, A. Descamps-Mandine, A. Ouerghi, M. G. Silly, S. Ithurria and E. Lhuillier, *ACS Appl. Nano Mater.*, 2022, **5**, 8602. DOI 10.1021/acsanm.2c02103
19. B. Wang, M. Yuan, J. Liu, Z. Zhang, J. Liu, J. Yang, L. Gao, J. Zhang, J. Tang and X. Lan, *Nano Lett.*, 2024, **24**, 9583. DOI 10.1021/acs.nanolett.4c02235
20. B. Martinez, J. Ramade, C. Livache, N. Goubet, A. Chu, C. Gréboval, J. Qu, W. L. Watkins, L. Becerra, E. Dandeu, J. L. Fave, C. Méthivier, E. Lacaze and E. Lhuillier, *Adv. Opt. Mater.*, 2019, **7**, 1900348. DOI 10.1002/adom.201900348
21. X. Tang, M. M. Ackerman, G. Shen and P. Guyot-Sionnest, *Small*, 2019, **15**, 1804920. DOI 10.1002/sml.201804920
22. M. M. Ackerman, M. Chen and P. Guyot-Sionnest, *Appl. Phys. Lett.*, 2020, **116**, 083502. DOI 10.1063/1.5143252
23. P. Rastogi, A. Chu, T. H. Dang, T. Prado, C. Gréboval, J. Qu, C. Dabard, A. Khalili, E. Dandeu, B. Fix, X. Z. Xu, S. Ithurria, G. Vincent, B. Gallas and E. Lhuillier, *Adv. Opt. Mater.*, 2021, **9**, 2002066. DOI 10.1002/adom.202002066
24. X. Tang, M. M. Ackerman, M. Chen and P. Guyot-Sionnest, *Nat. Photonics*, 2019, **13**, 277. DOI 10.1038/s41566-019-0362-1
25. P. Rastogi, E. Izquierdo, C. Gréboval, M. Cavallo, A. Chu, T. H. Dang, A. Khalili, C. Abadie, R. Alchaar, S. Pierini, H. Cruguel, N. Witkowski, J. K. Utterback, T. Brule, X. Z. Xu, P. Hollander, A. Ouerghi, B. Gallas, M. G. Silly and E. Lhuillier, *J. Phys. Chem. C*, 2022, **126**, 13720. DOI 10.1021/acs.jpcc.2c02044
26. J. Yang, H. Hu, Y. Lv, M. Yuan, B. Wang, Z. He, S. Chen, Y. Wang, Z. Hu, M. Yu, X. Zhang, J. He, J. Zhang, H. Liu, H.-Y. Hsu, J. Tang, H. Song and X. Lan, *Nano Lett.*, 2022, **22**, 3465. DOI 10.1021/acs.nanolett.2c00950
27. J. Yang, Y. Lv, Z. He, B. Wang, S. Chen, F. Xiao, H. Hu, M. Yu, H. Liu, X. Lan, H.-Y. Hsu, H. Song and J. Tang, *ACS Photonics*, 2023, **10**, 2226. DOI 10.1021/acsp Photonics.2c01145
28. H. H. Ku, *J. Res. Natl. Bur. Stand. C Eng. Inst.*, 1966, **70C**, 263. DOI 10.6028/jres.070C.025